Title : Optimized arrays for 2-D resistivity surveys with combined surface and buried arrays

Authors : M. H. Loke[1*], H. Kiflu[2], P.B.Wilkinson[3], D. Harro[4], and S. Kruse[2]

[1] Geotomo Software, 115 Cangkat Minden Jalan 5, Minden Heights, Gelugor 11700, Penang, Malaysia

[2] Department of Geology, University of South Florida, 4202 E. Fowler Avenue, SCA 528, Tampa, FL 33620-8100, USA

[3] British Geological Survey, Kingsley Dunham Centre, Keyworth, Nottingham, United Kingdom NG12 5GG

[4] Geo3Group, 2509 Success Drive, Suite 1, Odessa, FL 33556, USA

[*] Corresponding author, email : drmhloke@yahoo.com

Abstract

The ‘Compare R’ method is used to automatically generate optimized arrays for 2-D resistivity surveys with electrodes arranged along parallel lines on the surface and the subsurface. The resolution at depth is greatly improved by carrying out measurements with at least one line of electrodes below the surface using a direct push installation technique. The performance of the optimized arrays is compared with a standard measurement sequence created manually that was used for previous surveys. Tests were conducted using a synthetic model and a field survey in an area with karst geology that has some ground truth. Both tests show that the optimized arrays have significantly better resolution compared with a standard measurement sequence. We also show that artefacts in the inversion model can be reduced by using higher damping factors near the positions of the subsurface electrodes.

Keywords : Resistivity, tomography, optimized, deep, arrays

INTRODUCTION

In the last twenty-five years there have been major developments in the resistivity method such that it can provide realistic images in geologically complex areas. Developments in multi-electrode resistivity meter systems (Griffiths *et al.*, 1990; Dahlin, 1996) and rapid inversion software (Loke and Barker, 1996a,b) have led to the widespread use of two-dimensional (2-D) and even three-dimensional (3-D) resistivity surveys (White *et al.*, 2001; Auken *et al.*, 2006; Loke *et. al.*, 2014b). It is now widely used in engineering, environmental and mineral exploration surveys (Chambers *et al.*, 2006; Loke *et al.*, 2013).

One of the main weaknesses of the resistivity method is that the resolution of surveys carried out with electrodes on the ground surface decreases rapidly with depth. Thus cross-borehole surveys have been carried out to improve the resolution across a larger depth range (LaBrecque *et al.*, 1996; Slater *et al.*, 2000; Wilkinson *et al.*, 2006a; Chambers *et al.*, 2010). Most cross-borehole surveys use electrodes laid out along vertical boreholes where the vertical extent of the area of interest is larger than the horizontal extent. For some geological problems, such as mapping of sinkholes (Kruse *et al.*, 2006), the main interest is to map a region of a long horizontal extent. But surveys with electrodes on the ground surface are limited to a maximum depth of investigation, even with optimized arrays (Loke *et al.*, 2015), that is less than one-third the line length. If the line length is limited by access, as is often the case in urban environments, the target features may lie below the depth of investigation. Furthermore surface arrays have very limited depth of investigation at the ends of the arrays. One innovative technique for increasing depth of penetration while maintaining horizontal extent across the line length

is to use electrodes arranged along two parallel horizontal lines, with one line of electrodes placed below the surface (Harro and Kruse, 2013). This array is analogous to a cross-borehole array, turned on its side, with one set of electrodes on the surface and the other directly beneath it. Similar surveys have been made with electrodes on the surface and in a tunnel or horizontal boreholes (Danielsen and Dahlin, 2010; Simyrdanis *et al.*, 2014; Power *et al.*, 2015).

The sub-surface electrodes can be rapidly and inexpensively installed using a direct push installation technique (Harro and Kruse, 2013). Nevertheless, the time and cost to install the buried electrodes is greater than that required to make the resistivity measurements, so it is critical to maximize the information that can be obtained from readings involving these subsurface electrodes. In this paper we use automatic array optimization techniques (Wilkinson *et al.*, 2006b; Loke *et al.*, 2010a,b) to find optimal sets of readings for this survey geometry. It has been shown that array optimization techniques can significantly improve the resolution obtained compared with traditional array geometries, including electrodes on the ground surface (Stummer *et al*., 2004; Nenna *et al.*, 2011; Wilkinson *et al.*, 2012), vertical boreholes (Coscia *et al.*, 2008; Hagrey and Petersen, 2011; Hagrey, 2012; Loke *et al.*, 2014a) and between the surface and a tunnel (Simyrdanis *et al.*, 2014). The 'Compare R' (CR) algorithm proved to be the method that generated arrays with the highest resolution among the techniques that were tested by Loke *et al.* (2010a).

The following sections describe the direct push installation technique and the ‘Compare R’ array optimization method, followed by an algorithm to generate the test arrays for this type of survey using subsurface electrodes along horizontal lines. A

method to reduce artefacts in inversion models for data from surveys with subsurface electrodes is described. We then compare the performance of the optimized arrays with a 'standard' measurement sequence (Harro and Kruse, 2013) using model resolution sections and a synthetic model data set. Finally results from a field survey are presented.

DIRECT PUSH INSTALLATION TECHNIQUE

We refer to the installation of matching surface and buried arrays as MERIT, for Multi-Electrode Resistivity Implant Technique. With MERIT, the subsurface electrodes are implanted using a Geoprobe (Direct-Push) system (e.g. United States Environmental Protection Agency, 2005) (Figure 1). The implanted electrode is an expendable drive point with an attached wire (Harro and Kruse, 2013). The drive point is placed in the lower end of a groundwater sampling sheath that is driven downwards by percussion. When it reaches the desired depth, the sheath is withdrawn leaving the implanted electrode joined to the surface by the attached wire. Up to about 150 linear meters of implant installation can be performed in a single day, for electrode spacings of 10 meters. Installation is less expensive and more rapid than conventional vertical boreholes. Comparing MERIT installation costs with those of vertical boreholes, a MERIT array with 14 buried electrodes at 7.6 meters depth can be installed for less than the price of two boreholes, each with a 15-electrode string (United States Environmental Protection Agency, 1998). Thus MERIT is clearly an attractive choice for deeper targets with large horizontal extent.

The vertical accuracy in the position of the implanted electrode is expected to be similar to that of an electrode mounted on a rigid support in a vertical borehole (e.g. Wilkinson et al., 2008). The lengths of the push rods for installation can be accurately measured, and the controlled hydraulics on a direct push rig permit advancement in increments as small as 0.125 cm. The horizontal uncertainty in electrode position is a function of deviation of the direct push rod from vertical. Following Paasche et al. (2009) we consider a 5 degree deflection from verticality as a worst-case scenario. The horizontal position error is then

<~0.087 x depth; or <~60 cm for electrodes at 7 m depth. In soft sediments, deflections from vertical are expected to be much less than this worst-case scenario.

THEORY

Data inversion, model resolution and the 'Compare R' method

The smoothness-constrained least-squares optimization method is frequently used for 2-D inversion of resistivity data (Ellis and Oldenburg, 1994; Loke *et al.*, 2003). The subsurface model commonly consists of a large number of rectangular cells where the size and positions of the cells are fixed but the resistivity is allowed to vary. The linearized least-squares equation that gives the relationship between the model parameters and the measured data is given below.

$$\left(\mathbf{G}^{\mathbf{T}}\mathbf{G}+\lambda\mathbf{W}^{\mathbf{T}}\mathbf{W}\right)\Delta\mathbf{r}_{\mathbf{i}}=\mathbf{G}^{\mathbf{T}}\mathbf{d}-\lambda\mathbf{W}^{\mathbf{T}}\mathbf{W}\,\mathbf{r}_{\mathbf{i-1}}, \qquad (1)$$

where $\Delta\mathbf{r}_{\mathbf{i}}=\mathbf{r}_{\mathbf{i}}-\mathbf{r}_{\mathbf{i-1}}$. The Jacobian matrix **G** contains the sensitivities of the (logarithm of) calculated apparent resistivity values with respect to the model parameters (the logarithm of the model resistivity values). **W** contains the roughness filter constraint, λ is the damping factor and **d** is the data misfit vector. $\mathbf{r}_{\mathbf{i-1}}$ is the model parameter vector for the previous iteration, while $\Delta\mathbf{r}_{\mathbf{i}}$ is the change in the model parameters. Various modifications have been made to the above equation to incorporate desired characteristics in the data misfit or model roughness, such as using a L1-norm criterion for the data misfit and model roughness filter (Loke *et al.*, 2003) and to include known data errors using a data weighting matrix (Ellis and Oldenburg, 1994). It can be shown that the model resolution matrix **R** (Menke, 1989; Loke *et al.*, 2010a) is given by

$$\mathbf{R} = \mathbf{B}\ \mathbf{A}\ \text{, where}\quad \mathbf{A} = \mathbf{G}^{\mathbf{T}}\mathbf{G} \text{ and } \mathbf{B} = \left(\mathbf{G}^{\mathbf{T}}\mathbf{G} + \lambda \mathbf{W}^{\mathbf{T}}\mathbf{W}\right)^{-1} . \qquad (2)$$

The main diagonal elements of **R** give an estimate of the model cells' resolution.

The 'Compare R' method (Wilkinson *et al.*, 2006b) attempts to determine the set of array configurations that will maximize the average resolution value for a homogeneous earth model. For a system with *N* electrodes, there are $N(N\text{-}1)(N\text{-}2)(N\text{-}3)/8$ independent four-electrode configurations. To reduce the number of possible configurations, 'gamma' type arrays where the current and potential electrodes are interleaved (Carpenter and Habberjam, 1956), and those with large geometric factors that exceed a set limit are excluded (Stummer *et al.*, 2004). The remaining configurations form the 'comprehensive' data set. A small base data set consisting of the dipole-dipole configurations with the '*a*' dipole length of 1 unit electrode spacing is used as the starting base data set. The change in the model resolution matrix **R** for each new array when added to the base set is then calculated. A selected number of the configurations that result in the largest increase in the model resolution, and have a suitable degree of orthogonality to the existing configurations, are then added to the base data set (Wilkinson *et al.*, 2012). This is repeated until the desired number of optimized array configurations is selected.

The Sherman-Morrison Rank-1 update (Golub and van Loan, 1989) is used to calculate the change in the model resolution matrix when a new test configuration is added to the base set. The following set of updating formulae (Loke *et al.*, 2010b) is used to calculate the new resolution matrix $\mathbf{R_{b+1}}$ when a new array is added to the base set

$$\mathbf{R_{b+1}} = \mathbf{R_b} + \Delta\mathbf{R_b},$$

where $\Delta\mathbf{R_b} = \frac{\mathbf{z}}{1+\mu}\left(\mathbf{g}^{\mathrm{T}} - \mathbf{y}^{\mathrm{T}}\right)$, (3)

and $\mathbf{z} = \mathbf{B_b g}$, $\mathbf{y} = \mathbf{A_b z}$ and $\mu = \mathbf{g.z}$.

The vector **g** contains the sensitivity values of the model cells for the new test configuration. Equation (3) provides a computationally efficient method to calculate the change in the model resolution (Loke *et al.*, 2015).

The following function F_{CR} (Wilkinson *et al.*, 2012) that uses the ratio of the change in the model resolution to the comprehensive data set resolution is used to rank the improvement in the model resolution with *m* model cells due to an add-on array.

$$F_{CR} = \frac{1}{m}\sum_{j=1}^{j=m}\frac{\Delta R_b(j,j)}{R_c(j,j)}. \quad (4)$$

R_b and R_c are the base and comprehensive data set model resolutions. The 'Compare R' method selects the arrays that have the largest F_{CR} values. The average relative model resolution is given by

$$S_r = \frac{1}{m}\sum_{j=1}^{j=m}\frac{R_b(j,j)}{R_c(j,j)}. \quad (5)$$

This is used to assess the performance of the array optimization methods.

The combined effects of computer software and hardware improvements over the past few years has reduced the calculation time to generate the optimized arrays by several orders of magnitude (Loke *et al.*, 2015). The cost to install the subsurface electrodes in field surveys (Harro and Kruse, 2013) is much greater than that required to calculate the optimized arrays. Thus in this paper we use the 'single step' algorithm (Loke *et al.*, 2010b) of the ‘Compare R’ method to generate the optimized arrays in order to get the best possible resolution for the same number of measurements. In the 'single-step'

algorithm, only the array (or symmetrical pair of arrays) that gives the largest increase in the model resolution is added to the base data set after each iteration. Currently, it takes less than a minute to generate the optimized arrays with 400 to 800 readings for 2-D surveys with 28 electrodes used for such field surveys.

A method to generate test arrays for the comprehensive data set

It was observed by Wilkinson *et al.* (2008) that certain cross-borehole configurations for vertical boreholes are extremely sensitive to errors in the electrodes positions. An initial attempt to calculate optimized arrays for arrays with subsurface electrodes showed that negative apparent resistivity values can occur, even for simple models such as that shown in Figure 2. The problem of unstable arrays increases as the ratio of the distance between the two lines of electrodes to the length of the survey lines decreases below 1.0. The setup shown in Figure 2 has a distance to length ratio of 0.19, thus making it particularly sensitive to this problem.

The geometric factor is used to filter out arrays that are likely to be unstable for surveys with electrodes on the ground surface. However this is insufficient for surveys with subsurface electrodes. To distinguish arrays that are stable from those that are potentially unstable, Wilkinson *et al.* (2008) used the ratio of the sensitivity of the geometric factor to position errors to the geometric factor value. The geometric factor K for any four electrode array is given by

$$K = 4\pi / \left[\frac{1}{r_{AM}} - \frac{1}{r_{AN}} - \frac{1}{r_{BM}} + \frac{1}{r_{BN}} + \frac{1}{r_{A'M}} - \frac{1}{r_{A'N}} - \frac{1}{r_{B'M}} + \frac{1}{r_{B'N}} \right]. \quad (6)$$

The current electrodes are denoted by A and B, while the potential electrodes are M and N. r_{AM} is the distance between A and M. A' and B' represent the location of the images

above the ground surface of the current electrodes if they are below the surface. Assuming all the electrodes are located along the *y=0* plane for a 2-D survey, the location of the *A* electrode is given by (x_A,z_A). The sensitivity of the geometric factor to errors in the position of the *A* electrode can be calculated using the following equation.

$$\left(\frac{\partial K}{\partial A}\right)^2 = \left(\frac{\partial K}{\partial x_A}\right)^2 + \left(\frac{\partial K}{\partial z_A}\right)^2 \tag{7}$$

The overall sensitivity *s* of *K* to errors in the positions of all the four electrodes is then obtained by summing up the individual contributions.

$$s^2 = \left(\frac{\partial K}{\partial A}\right)^2 + \left(\frac{\partial K}{\partial B}\right)^2 + \left(\frac{\partial K}{\partial M}\right)^2 + \left(\frac{\partial K}{\partial N}\right)^2 \tag{8}$$

The relative error in *K* (Wilkinson *et al.*, 2008) is then defined to be

$$R_E = s / K . \tag{9}$$

We note that *s* is a dimensionless quantity that depends only on the relative positions of the electrodes. It does not change with the electrode spacing. For example, the Wenner array will always have a value of 1.295 regardless of the '*a*' spacing between the electrodes. However, the geometric factor *K* depends on the electrode spacing. Thus the value of R_E that is used to filter the potentially unstable arrays should be adjusted accordingly.

Wilkinson *et al.* (2008) demonstrated using potential values calculated analytically for a model with a vertical contact that some of the 'unstable' array configurations can also give rise to negative apparent resistivity values. Here, we give a semi-quantitative explanation for the occurrence of negative apparent resistivity values for a more general model such as in Figure 2. To a first approximation, the apparent

resistivity value ρ_b obtained when a model cell is changed by $\Delta\rho$ from a homogeneous background value ρ_0 is given by

$$\rho_b \approx \rho_0 + \frac{\partial \rho_a}{\partial \rho}\Delta\rho \qquad (10)$$

In situations when the sensitivity value $\frac{\partial \rho_a}{\partial \rho}$ is positive and $\Delta\rho$ is negative (or vice versa), the contribution from the perturbation term $\frac{\partial \rho_a}{\partial \rho}\Delta\rho$ is negative. If it is sufficiently large (and assuming linear instead of logarithmic quantities are used), ρ_b can become negative. Figure 3 shows a plot of the sensitivity values $\frac{\partial \rho_a}{\partial \rho}$ for four example test arrays. The arrays in Figures 3a and 3b are 'stable' arrays with positive apparent resistivity values, while those in Figures 3c and 3d can give rise to negative values. Note that while the array in Figure 3a (a subsurface inline dipole-dipole array) has the largest geometric factor (8311 m.), it has lower values of the geometric factor relative error (1.1 m^{-1}) and the maximum sensitivity value for an individual model cell $\left|\frac{\partial \rho_a}{\partial \rho}\right|$ of 0.17. In comparison although the array configuration in Figure 3c (that can give rise to negative apparent resistivity values) has a smaller geometric factor of 3603 m., it has much higher values of 21.9 m^{-1} and 4.54 for the geometric factor relative error and maximum model cell sensitivity values.

In creating the comprehensive data sets, we set maximum limits for the geometric factor as well as the geometric factor relative error in filtering out arrays that are likely to be unstable. Many of the unstable arrays were found to have only one current electrode

located in between the potential electrodes (or one potential electrode between current electrodes) such as in Figure 3c. To avoid this situation, we use a slight modification of the algorithm used by Loke *et al.* (2014c) for 3-D surveys to automatically generate the comprehensive data set arrays. The arrays consist of offset versions of the conventional inline 'alpha' and 'beta' configurations. Figures 4a to 4d show the different permutations for arrays of the 'alpha' type with an *A*-*M*-*N*-*B* configuration. Firstly, we start with all the four electrodes in the upper survey line (Figure 4a). The *B*, *M* and *N* electrodes are then shifted step by step to the lower survey line. A corresponding set of the 'alpha' arrays are also generated starting with all the four electrodes in the lower survey line (Figure 4e) which are then shifted step by step to the upper survey line. A similar method is used to generate arrays of the 'beta' type with the *B*-*A*-*M*-*N* configuration. Another set of configurations with the two middle electrodes on a separate line (Figure 4f) are also included in the set of possible arrays. We also include arrays with an 'equatorial dipole-dipole' configuration in the comprehensive data set (Figures 4g and 4h).

A method to reduce artifacts in inversion models with subsurface electrodes

It was observed by Ellis and Oldenburg (1994) that the inversion of data collected using electrodes in vertical boreholes tends to produce artifacts near positions of the subsurface electrodes. This was because the model cells near the positions of the electrodes have higher sensitivity values, and the least-squares inversion algorithm tends to preferentially modify the resistivity values of these model cells in an attempt to reduce the data misfit. A similar effect was observed for data collected using arrays with subsurface electrodes where the inversion model tends to produce linear features along

the bottom row of electrodes. The solution proposed by Ellis and Oldenburg (1994) was to modify the equation (1) into the following form using spatially varying damping factor.

$$\left(\mathbf{G}^{\mathbf{T}}\mathbf{G} + \lambda \mathbf{W}^{\mathbf{T}}\mathbf{M}\,\mathbf{W}\right)\Delta\mathbf{r}_{\mathbf{i}} = \mathbf{G}^{\mathbf{T}}\mathbf{d} - \lambda \mathbf{W}^{\mathbf{T}}\mathbf{M}\,\mathbf{W}\,\mathbf{r}_{\mathbf{i-1}} \qquad (11)$$

$\mathbf{M}$ is a diagonal matrix with diagonal elements containing the relative damping factor weight associated with each model cell. In the method used by Ellis and Oldenburg (1994), the diagonal elements of **M** have relatively small values within a defined region of interest, and larger values elsewhere. This effectively constrains the inversion algorithm to produce a model with resistivity variations within the region of interest. In the survey problem considered in the paper, there is no defined region of interest but we would like to suppress large variations in the model resistivity values near the positions of the electrodes. We thus use the following equation to set the diagonal element m_k associated with the kth model cell.

$$m_k = 1.0 + 5.0 \exp\left(-\left[\frac{d_k}{s}\right]^2\right) \qquad (12)$$

d_k is the distance of the center of the model cell from the nearest electrode while s is the unit electrode spacing. This function effectively imposes a larger damping factor on model cells that are near an electrode, while at large distances from the electrodes it approaches that of the background damping factor value λ. The use of relatively larger damping factors for cells near the electrodes compensates for the decrease of the cell sensitivity values with distance from the electrodes. Tests with a number of synthetic models suggest that using a factor of about 5.0 in equation (12) provides a reasonable

balance between suppressing artefacts while still allowing the detection of real anomalies near the electrodes.

RESULTS

Model resolution tests

As an example, we examine the case with two parallel lines with 14 electrodes with an inline spacing of 2 meters placed on the surface and at a depth of 5 meters. The x-position of the electrodes range from 6 to 32 meters in the model discretization used (Figure 2). It was shown by Loke *et al.* (2014a) that for cross-borehole surveys, the region outside the area between the boreholes can have significant model resolution values. Thus for the model resolution calculations, the model cells extend in the x-direction to 6 meters beyond the ends of the lines, while the maximum model depth extends to 9 meters below the lower survey line. The subsurface is subdivided into 560 cells each with a 1 by 1 meter cross-sectional area. We use cell widths of half the unit electrode spacing as recommended by Sasaki (1992) for cross-borehole surveys. A value of 0.001, which is similar to that used in the data inversion, was used for the damping factor in equation (2). In the model resolution and synthetic data inversion tests, we use a measurement sequence with 446 array configurations created manually (Harro and Kruse, 2013) as the 'standard' array data set for comparison. It consists of inline Wenner and dipole-dipole arrays for the surface array and buried array, the same geometries with

current and potential measurements being made at different depths (for example, current electrodes at the surface array, potential electrodes at the buried array), and the equatorial dipole arrangements of Figures 4g and 4h. The maximum geometric factor in this data set is about 3400 m. which is also used as the cutoff value for optimized arrays. Wilkinson *et al.* (2008) used a cutoff value of 5 m^{-1} for the geometric factor relative error R_E for a vertical boreholes survey with an electrode spacing of 1 meter. Since the test configuration in Figure 2 has an electrode spacing of 2 meters, we use a cutoff value of 2.5 for R_E. This produces a comprehensive data set with 19897 possible arrays.

Figure 5 shows the change in the average relative model resolution S_r (equation 5) for the optimized arrays generated using the 'Compare R' single-step algorithm with the number of data points. For comparison, we also show a similar plot for the optimized arrays using a block algorithm (Loke *et al.*, 2010b) where the size of the base data set is increased by 5% after each iteration. The results are similar to that obtained earlier for surveys along the ground surface (Loke *et al.*, 2010b) and across vertical boreholes (Loke *et al.*, 2014a). The initial base data set that consists of the inline dipole-dipole arrays along the two lines (with the '*a*' dipole length of 2 m.) has 107 data points. There is a rapid increase in the model resolution for the first 800 data points followed by a slower increase. The model resolution for the single-step optimized data set is significantly higher than that for the block algorithm set for small data sets of less than 800 data points. Above 1200 data points, both curves converge to almost similar values.

The model resolution section for the comprehensive data set is shown in Figure 6a. Since the comprehensive data set includes all the viable arrays, it shows the maximum resolution that can be achieved by the survey arrangement. Note that the cells at the edges

of the model section have resolution values that are less than 0.02. This shows that all the regions of the subsurface that have significant resolution values are included in the model. Not surprisingly, the regions with the highest model resolution values are concentrated around the survey lines where the electrodes are located. Most of the area between the survey lines have relatively high resolution values of above 0.7 near the central region. The resolution values gradually decrease towards the ends of the lines. The regions with resolution values of up to 0.05 extend to about 4 meters laterally beyond the ends of the lines, and up to 4 meters below the bottom survey line.

The model resolution for the 'standard' measurement sequence is shown in Figure 6b. The average model resolution value for the standard arrays is 0.192 that is much lower than the value of 0.288 for the comprehensive data set. The model resolution section for the optimized data set (using the single-step method) with 447 data points is shown in Figure 6c. It has one extra data point above the target of 446 arrays due to the requirement that it includes the symmetrical counterpart of each array (Loke *et al.*, 2010a). The average resolution value of 0.247 obtained with the optimized data set is significantly higher than for the standard arrays. The resolution values are significantly higher in the central region between the survey lines where the optimized data set has resolution values of about 0.5 compared to below 0.3 for the standard arrays. We also show the model resolution section for an optimized data set with 851 data points (Figure 6d). The main effect of increasing the number of data points seems to be a slight increase in the average model resolution from 0.247 to 0.258.

The differences in the resolutions achieved by the different data sets are more clearly shown in plots of the relative model resolution sections $\frac{R_b(j,j)}{R_c(j,j)}$ in Figure 7. The

optimized data set with 447 data points achieves higher values of about 0.7 (Figure 7b) in the central region between the two lines compared to about 0.4 for the standard data set (Figure 7a). The resolution ratio value at the same region is increased to about 0.8 for the optimized arrays with 851 data points (Figure 9c). The resolution ratio values are also significantly higher near the ends of the survey lines for the optimized data sets. The higher resolution values achieved by the optimized data set with 851 data points (Figure 7c) compared to the smaller optimized data set (Figure 7b) below the subsurface survey line are also more clearly shown in the relative resolution sections.

LaBrecque *et al.* (1996) recommended a maximum separation of 0.75 times the borehole array length for vertical boreholes. The resolution of the central region between the lines of electrodes decreases with increasing distance between the lines. Previous studies show that the maximum depth of investigation (using optimized arrays) of a line of electrodes on the ground surface is about one-quarter to one-third the line length (Loke *et al.*, 2015). Thus the maximum possible separation between the two lines of electrodes to obtain reasonable overlap between the areas with significant resolution is probably about one-half the line length. However, in most field surveys, a limit of about 0.2 times the line length was used for the separation between the lines to ensure the region with significant resolution extends across most of the line length. We note that the ratio of the line separation and length is about 0.19 for the synthetic example and 0.15 for the field example in the following sections of the paper.

Tests with a synthetic model

The test model consists of five rectangular blocks embedded in a homogeneous background medium of 100 ohm.m (Figure 2). The apparent resistivity values were calculated for the standard arrays with 446 data points, and the optimized data sets with 447 and 851 data points using a finite-element forward modeling program. Voltage-dependent random noise (Zhou and Dahlin, 2003) with an average amplitude of 1 milli-ohm was added to the resistance values before they were multiplied by the geometric factors to convert them to apparent resistivity values. For the resulting apparent resistivity values, the noise level is smaller when the geometric factor is smaller. An inversion of the apparent resistivity data sets was then carried out using a least-squares optimization program (Loke *et al.*, 2003). We used the L1-norm constraint for both the data misfit and spatial model roughness in the inversion of the data set based on the blocky nature of the targets. The use of the L1-norm method for the data misfit makes the inversion procedure less sensitive to noise (Farquharson and Oldenburg, 1998). The L-curve method was used to automatically select the optimum damping factor (Farquharson and Oldenburg, 2004; Loke *et. al.*, 2014b) in equation (1). The method to reduce artefacts by using higher damping factors for the model cells near the electrodes described in a previous section was also used. The inversion routine usually converges in 3 or 4 iterations after which there were no significant changes in the data misfit.

The resulting inversion models are shown in Figure 8. The data misfit for the standard data set at 0.5% is slightly lower than for the optimized data sets (1.4% and 1.0%). This is probably partly due to the smaller average geometric factor for the arrays used in the standard data set (499 m.) compared to the optimized data sets (1148 and 1086 m. respectively for the smaller and larger data sets). A similar pattern was observed

for surface and cross-borehole surveys (Loke *et al.*, 2010a; Loke *et al.*, 2014a) where the array optimization method tends to select arrays with larger geometric factors.

The topmost high resistivity block (block 1 in Figure 2) is detected by all the inversion models. However, the larger optimized data set model achieves the highest maximum resistivity value of 399 ohm.m (true value 500 ohm.m) compared to 346 ohm.m and 332 ohm.m for smaller optimized and standard data sets (Figure 8) The low resistivity block (number 2 in Figure 2) near the left end of the survey lines is not well resolved in the standard data model (Figure 8a) compared to the optimized data sets (Fugure 8b and 8c). It is slightly better defined in the larger optimized data set model (Figure 8c). The low resistivity block 3 located between the two lines (Figure 2) is well defined in all the models. Blocks 4 and 5 located below the lower survey line are detected in all the inversion models. Block 5 is significantly better resolved in the optimized data sets models. They give maximum values of 233 ohm.m and 273 ohm.m for the smaller and larger optimized data set models, compared to 153 ohm.m for the standard data set model.

To quantitatively demonstrate the differences in the accuracy of the models, we also calculate the root-mean-squared model misfits between the true (r_t) and the calculated (r_c) model values using the following equation.

$$\delta = \left(\frac{1}{m} \sum_{i=1}^{m} \left[\log(r_t(i)) - \log(r_c(i)) \right]^2 \right)^{0.5} \qquad (12)$$

Note the difference between the logarithms of the true and inversion model resistivity values at the model cells is used. The standard data set model gives the largest model misfit of 0.208 followed by the smaller optimized data set with 0.184 and the larger

optimized data set at 0.173. Although the optimized data sets have higher data misfits than the standard data set, they produce models that are more accurate.

Figure 8d shows the inversion model for the standard data set where the inversion was carried out using a uniform damping factor for all the model cells. The inversion model has a slightly higher model misfit of 0.210. The anomaly corresponding to the high resistivity block below the subsurface electrodes is elongated along direction of the line. The low resistivity block to the left of the lines is significantly less well resolved (Figure 8d) compared to the model obtained using the spatially varying damping factor (Figure 8a). It was observed during the inversion process that the model tends to develop artefacts near the subsurface electrodes in the first few iterations which are not completely removed in the later iterations. This is probably because of the local optimization (Gauss-Newton) method used. The optimization path taken by the inversion process is strongly influenced by the higher sensitivity (Jacobian matrix) values for the model cells near the subsurface electrodes.

It was shown by Loke *et al.* (2014a) that plots of the point spread function (Friedel, 2003; Miller and Routh, 2007; Oldenborger and Routh, 2009) help to explain the behaviour of different data sets for cross-borehole surveys. If the data set has perfect resolution, the spread function will have a value of 1.0 at the location of the cell and 0.0 elsewhere. In this paper, we plot the spread function values for a model cell at (5.5,3.5) located within block 2 near the left end of the survey lines. Figure 9a shows the spread function plot for the comprehensive data set. The spread function contours show an elliptical pattern with a narrow width in the x-direction but a wider spread in the z-direction. Thus we would expect the horizontal position of an anomaly at this location to

be more accurately determined than its vertical position. In fact, the maximum of the spread function plot is located 1 meter below the actual position of the model cell. The spread function plots for the optimized data sets (Figures 9c and 9d) are similar to those of the comprehensive data set except they have lower amplitudes. The spread function plots explains why the horizontal position of the anomaly corresponding to block 2 in the inversion models for the optimized data sets are close to the true position, but the vertical position of the lowest resistivity value is offset downwards (Figures 8b and 8c). The spread function plot for the standard data set (Figure 9b) has a broader maximum and significantly lower amplitude. Thus block 2 is expected to be significantly less well resolved in the standard data set model compared to the optimized data sets, as shown in Figure 8a.

Field Test

A case study profile was conducted at the Geopark research site on University of South Florida campus in west-central Florida, United States (Figure 10). The site is characterized by karstified limestone bedrock overlain by about 5 meters of overburden soils (Figure 11). The overburden consists of granular sands over more cohesive sandy clay and clay soil, with clay content generally increasing with depth. Depths to contacts were mapped along the first 33m of this profile with a suite of 3 standard penetration tests (SPTs) (Figure 11) and 5 cone penetration tests (CPTs) (Stewart and Parker, 1992). The data show an irregular zone of sediments to greater than 12 m depth at approximately the 24 m and 30 m marks along the profile. These are interpreted as sediment-filled dissolution cavities beneath an overlying ravelling zone (Figure 11). A ground

penetrating radar survey (GPR) shows a depression in sandy layer centered approximately over the ravelling zone at 30 m along the profile (Figure 11). This GPR reflection corresponds to an increase in clay content within the unit characterized as sand by Stewart and Parker (1992). Solid lines indicate where depths to contacts are well established by CPTs, SPTs, or GPR data. Dashed lines indicate where contacts have been extrapolated. Although depths to sediment contacts are relatively well established over the first 33 meters of the line, the upper and lower boundaries of the weathered limestone zone are not well determined. No deep data were available beyond the 33m mark on the profile. On the day of the surveys the water table was measured in a nearby well at 2.8 m depth. Heavy antecedent rains imply the vadose zone also had substantial moisture content, so in general high-porosity areas would be expected to have higher water content, and hence lower resistivity. From other work in this area (Kruse *et al.*, 2006), one would expect high resistivities associated with the drier surficial sands, lower resistivities associated with clay-rich zones, and higher resistivities at depth associated with competent limestone. Over the saturated ravelling zones and sediment-filled dissolution cavities one would expect lower resistivities than in neighbouring intact rock.

A deep array of 14 electrodes was implanted at 7.62 m below ground surface, with an electrode spacing of 4 m using direct push technology. A matching set of 14 electrodes was placed at the surface, directly above the implanted electrodes. Resistivity measurements were carried out using an AGI SuperSting R1 resistivity meter. The survey was run using the standard 446-measurement array and again with the 432 and 559 measurement optimized arrays. An initial inversion of the data sets gave very high data misfits of 15% for the standard data set, and 26% and 33% for the smaller and larger

optimized data sets. An examination of the differences between the measured and calculated apparent resistivity values showed that this was mainly caused by measured data points with very high resistivity values (over 1000 ohm.m) or very low (including negative) values. Most of the apparent resistivity values were between 10 and 100 ohm.m. The extreme values for some of the data points was probably caused by poor ground contact at some of the electrodes. An initial data processing was then carried out by removing data points with apparent resistivity values of over 200 ohm.m and negative values. This reduced the overall data misfits but there were still some bad data points left as shown by large misfits at these points. A second data processing step was carried out by removing data points where the calculated apparent resistivity values was less than half or more than twice the measured values (misfits of more than 100%). The final data sets had 405 data points for the standard arrays, and 403 and 514 data points for the two optimized arrays. The inversion models obtained after the second round of data processing had significantly lower overall data misfits, and structures that were more consistent (Figure 11) with the known geological information.

Figure 11 shows that on the left side of the profile (where good ground-truthing is available) where both the standard and optimized arrays detect the higher resistivities expected for the uppermost sand layer and the higher resistivities expected for competent limestone at depth. However, the depths and pattern of the anomalies in optimized array model shows better agreement with the depths to the layers and other structures revealed by the GPR, CPT and SPT measurements. The optimized array also yields a stronger resistivity gradient close to the mapped depth of the sand-to-sandy clay contact between the 26 and 48 m marks. Both standard and optimized arrays show a zone of low

resistivities between depths of 8 to 14 m depth near the 30 m mark. It is interesting that this cavity at 30 m corresponds to a distinctive resistivity low and an overlying depression in a GPR reflecting horizon. The cavity at 24 m lies directly below a depression in the GPR reflection interface. Combined, the resistivity and GPR data suggest that the cavity at 30 m may be "active" in the sense that it is a focus of ongoing depression and ravelling, with a lower resistivity (higher conduit/cavity porosity) than that of the neighbouring "inactive" feature at 24 m. The optimized array results, which are expected to have somewhat better resolution below the deep array (Figure 8), also more strongly indicate that the conduit/depression feature at 30 m extends to depth as a low-resistivity zone. Note the optimized arrays show the decrease in the thickness of the uppermost sand layer (as marked by the GPR reflector) towards the right end of the line more clearly (Figures 11b and 11c) than the standard arrays (Figure 11a). The conduit at the right end of the line is also more clearly marked by low resistivity values in the optimized arrays sections.

Figure 11d shows the inversion model for the standard arrays without the additional damping near the subsurface electrodes. Note the linear artefacts near the subsurface electrodes are more prominent, particularly between the 4 and 20 m marks, than in the model without the additional damping (Figure 11a).

Though use of the optimized array geometry improves resolution of several key features, the data has a higher noise level shown by the significantly larger data misfits. While the optimized data sets show more structures at depth, such as the low resistivity feature near the left end of the line, they need to be confirmed by ground truth. The array optimization procedure needs to be further refined, possibly by using lower limits for the

maximum geometric factor and its relative error, to avoid arrays that are more sensitive to noise and potentially less stable.

CONCLUSIONS

With multi-electrode resistivity surveys, it is almost always possible to take many more measurements than is practical, given survey time constraints. Most users in the early years of multi-electrode instruments deployed expanded versions of traditional 4-electrode array geometries. More recently it has been clearly demonstrated that improved imaging can be achieved, under time constraints, when optimal array geometries are selected (Stummer *et al.*, 2004; Wilkinson *et al.*, 2006b; Wilkinson *et al.*, 2012).

We demonstrate here how optimal array geometries can be found for a new array type, in which a deep array of electrodes is buried beneath a traditional surface 2-D array. The algorithm can be modified to generated optimized arrays for surveys where both lines of electrodes are installed below the surface (Danielsen and Dahlin, 2010). This array geometry has the potential to substantially increase depth resolution of resistivity surveys at sites where profile length is limited. With optimal arrays, significantly better resolution can be obtained not only for the space between the surface and deep arrays, but also for distances slightly beyond the lateral ends of the arrays, and for depths below the deep array. This improvement in resolution is documented with model resolution sections and a synthetic model. In particular, optimized array geometries better fit the amplitude of resistivity anomalies with dimensions on the scale of the electrode spacings. In a field test in covered karst terrain, inversion of optimal arrays produces better resolution of known features. The use of additional damping constraints for the model cells near the positions of the subsurface electrodes is necessary to reduce artefacts in the model near the electrodes. Further work is needed to develop optimal combinations of

array geometries and inversion procedures to fully exploit this method of combined deep and surface arrays. Reciprocal measurements should also be made (LaBrecque *et al.*, 1966) to better identify the 'noisy' data points and provided an estimate of the data error. We are also studying the optimum separation between the lines and the electrode spacing along the lines to maximize the survey region while obtaining reasonable resolution of the targets within this region. Further refinements to the method to reduce the artefacts near the subsurface electrodes using a spatially varying damping factor are being developed using additional synthetic models and field data sets. The Gauss-Newton method being a local optimization technique has the disadvantage of converging to a local minimum that is strongly dependent on the constraints used. The use of global optimization methods (Horst *et al.*, 2000) is being investigated to avoid this problem.

ACKNOWLEDGEMENTS

We are grateful to G3 Group –Forensic Consulting for providing equipment needed for collecting field data and installing deep electrodes. This paper is published with the permission of the Executive Director of the British Geological Survey (NERC).

REFERENCES

Auken E., Pellerin L., Christensen N.B. and Sørensen K. 2006. A survey of current trends in near-surface electrical and electromagnetic methods. *Geophysics* **71**, G249-G260.

Carpenter E.W. and Habberjam G.M. 1956. A tri-potential method of resistivity prospecting. *Geophysics* **11**, 455-469.

Chambers J.E., Kuras O., Meldrum P.I., Ogilvy R.O. and Hollands J. 2006. Electrical resistivity tomography applied to geologic, hydrogeologic, and engineering investigations at a former waste-disposal site. *Geophysics* **71**, B231-B239.

Chambers J.E., Wilkinson P.B., Wealthall G.P., Loke M.H., Dearden R., Wilson R. and Ogilvy R.D. 2010. Hydrogeophysical Imaging of Deposit Heterogeneity and Groundwater Chemistry Changes during DNAPL Source Zone Bioremediation. *Journal of Contaminant Hydrology* **118**, 43–61.

Coscia I., Marescot L., Maurer H., Greenhalgh S., and Linde N. 2008. Experimental Design for Crosshole Electrical Resistivity Tomography Data Sets. 14th European Meeting of Environmental and Engineering Geophysics. EAGE.

Dahlin T. 1996. 2D resistivity surveying for environmental and engineering applications. *First Break* **14**, 275-284.

Danielsen B.E. and Dahlin T., 2010. Numerical modeling of resolution and sensitivity of ERT in horizontal boreholes. *Journal of Applied Geophysics* **70**, 245–254.

Ellis R.G. and Oldenburg D.W. 1994. Applied geophysical inversion, *Geophysical Journal International* **116**, 5-11.

Farquharson C.G. and Oldenburg D.W. 1998. Nonlinear inversion using general measures of data misfit and model structure. *Geophysical Journal International* **134**, 213-227.

Farquharson C.G., and Oldenburg D.W. 2004. A comparison of automatic techniques for estimating the regularization parameter in non-linear inverse problems. *Geophysical Journal International* **156**, 411-425.

Friedel S. 2003. Resolution, stability and efficiency of resistivity tomography estimated from a generalized inverse approach, *Geophysical Journal International* **153**, 305–316.

Golub G.H. and van Loan C.F. 1989. *Matrix Computations (2nd edn)*. The John Hopkins University Press. ISBN 0801854148.

Griffiths D.H., Turnbull J. and Olayinka A.I. 1990. Two-dimensional resistivity mapping with a computer-controlled array. *First Break* **8**, 121-129.

Hagrey S. A. al and Petersen T. 2011. Numerical and experimental mapping of small root zones using optimized surface and borehole resistivity tomography. *Geophysics* **76**, G25-G35.

Hagrey S. A. al 2012. 2D optimized electrode arrays for borehole resistivity tomography and CO2 sequestration modelling. Pure and Applied Geophysics **169**, 1283-1292.

Harro D. and Kruse S. 2013. Improved imaging of covered karst with the multi-electrode resistivity implant technique, 13th Sinkhole Conference, NCKRI Symposium 2, Carlsbad, New Mexico, 7 pp.

Horst R., Pardalos P. M. and Thoai N. V. 2000. Introduction to Global Optimization (2nd ed.). Kluwer Academic, Dordrecht.

Kruse S., Grasmueck M., Weiss M. and Viggiano D. 2006. Sinkhole structure imaging in covered Karst terrain. *Geophysical Research Letters* **33**, L16405.

LaBrecque D.J., Miletto M., Daily W., Ramirex, A. and Owen E. 1996. The effects of noise on Occam's inversion of resistivity tomography data. *Geophysics* **61**, 538–548.

Loke M.H. Barker R.D. 1996a. Rapid least-squares inversion of apparent resistivity pseudosections using a quasi-Newton method. Geophysical Prospecting **44**, 131-152.

Loke M.H. Barker R.D. 1996b. Practical techniques for 3D resistivity surveys and data inversion. Geophysical Prospecting **44**, 499-523.

Loke M.H., Acworth I. and Dahlin T. 2003. A comparison of smooth and blocky inversion methods in 2D electrical imaging surveys. *Exploration Geophysics* **34**, 182-187.

Loke M.H., Wilkinson P. and Chambers J. 2010a. Fast computation of optimized electrode arrays for 2D resistivity surveys. *Computers & Geosciences* **36**, 1414-1426.

Loke M.H., Wilkinson P. and Chambers J. 2010b. Parallel computation of optimized arrays for 2-D electrical imaging. *Geophysical Journal International* **183**, 1202-1315.

Loke M.H., Chambers J.E., Rucker D. F., Kuras O. and Wilkinson P. B. 2013. Recent developments in the direct-current geoelectrical imaging method. *Journal of Applied Geophysics* **95**, 135-156.

Loke M.H., Wilkinson P., Chambers J. and Strutt, M. 2014a. Optimized arrays for 2-D cross-borehole electrical tomography surveys. *Geophysical Prospecting*, **62**, 172-189.

Loke M.H., Dahlin T., Rucker D.F. 2014b. Smoothness-constrained time-lapse inversion of data from 3-D resistivity surveys. *Near Surface Geophysics*, **12**, 5-24.

Loke M.H., Wilkinson P.B., Uhlemann S.S., Chambers J.E. and Oxby L. S. 2014c. Computation of optimized arrays for 3-D electrical imaging surveys. *Geophysical Journal International* **199**, 1751-1764.

Loke M.H., Wilkinson P.B., Chambers J.E., Uhlemann S.S. and Sorensen J.P.R. 2015. Optimized arrays for 2-D resistivity survey lines with a large number of electrodes. *Journal of Applied Geophysics* **112**, 136-146.

Menke W. 1989. *Geophysical data analysis: Discrete inverse theory (Revised edition)*. Academic Press Inc. IBSN 0124909213.

Miller C.R. and Routh P.S. 2007. Resolution analysis of geophysical images: Comparison between point spread function and region of influence measures. *Geophysical Prospecting* **55**, 835-852.

Nenna V., Pidlisecky A. and Knight R. 2011. Informed experimental design for electrical resistivity imaging, *Near Surface Geophysics* **9**, 469-482.

Oldenborger G.A. and Routh P.S. 2009. The point-spread function measure of resolution for the 3D electrical resistivity experiment. *Geophysical Journal International* **176**, 405-414.

Paasche H., Werban U. and Dietrich P.2009. Near-surface seismic traveltime tomography using a direct-push source and surface-planted geophones, *Geophysics*, **74** G17-G25.

Power C., Gerhard J.I., Tsourlos P., Soupios P., Simyrdanis K. and Karaoulis M. 2015. Improved time-lapse electrical resistivity tomography monitoring of dense non-aqueous phase liquids with surface-to-horizontal borehole arrays. *Journal of Applied Geophysics* **112**, 1-13.

Sasaki Y., 1992. Resolution of resistivity tomography inferred from numerical simulation. *Geophysical Prospecting* **40**, 453-464.

Simyrdanis K., Tsourlos P., Papadopoulos N. and Soupios P. 2014. Optimized Arrays for Surface-to-tunnel ERT Measurements. 20th European Meeting of Environmental and Engineering Geophysics, Athens, Greece, 14-18 September 2014, Tu PA1 02.

Slater L., Binley A.M., Daily W. and Johnson R. 2000. Cross-hole electrical imaging of a controlled saline tracer injection. *Journal of Applied Geophysics* **44**, 85-102.

Stewart M. and Parker J. 1992. Localization and seasonal variation of recharge in a covered karst aquifer system, Florida, USA, in Hydrogeology of Selected Karst Regions, H. Palos and W. Back, eds., *International Contributions to Hydrogeology* **13**, International Association of Hydrogeologists.

Stummer P., Maurer H. and Green A. 2004. Experimental design: Electrical resistivity data sets that provide optimum subsurface information. *Geophysics* **69**, 120-129.

United States Environmental Protection Agency 1998. Geophysical techniques to locate DNAPLs: Profiles of federally funded projects, EPA 542-R-98-020, Member Agencies of the Federal Remediation Technologies Roundtable, 31p.

United States Environmental Protection Agency 2005. Groundwater sampling and monitoring with direct push technologies, EPA 540/R-04/005, Office of Solid Waste and Emergency Response, 78p.

White R.M.S., Collins S., Denne R., Hee R. and Brown P. 2001. A new survey design for 3D IP modelling at Copper hill. *Exploration Geophysics* **32**, 152-155.

Wilkinson P.B., Chambers J.E., Meldrum P.I., Ogilvy R.D. and Caunt S. 2006a. Optimization of array configurations and panel combinations for the detection and imaging of abandoned mineshafts using 3D cross-hole electrical resistivity tomography. *Journal of Environmental and Engineering Geophysics* **11**, 213-221.

Wilkinson P.B., Meldrum P.I., Chambers J.E., Kuras O. and Ogilvy R.D. 2006b. Improved strategies for the automatic selection of optimized sets of electrical resistivity tomography measurement configurations. *Geophysical Journal International* **167**, 1119-1126.

Wilkinson P. B., Chambers J. E., Lelliott M., Wealthall P. and Ogilvy R. D. 2008. Extreme sensitivity of crosshole electrical resistivity tomography measurements to geometric errors. *Geophysical Journal International* **173**, 49-62.

Wilkinson P.B., Loke M.H., Meldrum P.I., Chambers J.E, Kuras O., Gunn D.A. and Ogilvy R.D. 2012. Practical aspects of applied optimised survey design for Electrical Resistivity Tomography. *Geophysical Journal International* **189**, 428-440.

Zhou B. and Dahlin T. 2003. Properties and effects of measurement errors on 2D resistivity imaging surveying. *Near Surface Geophysics* **1**, 105-117.

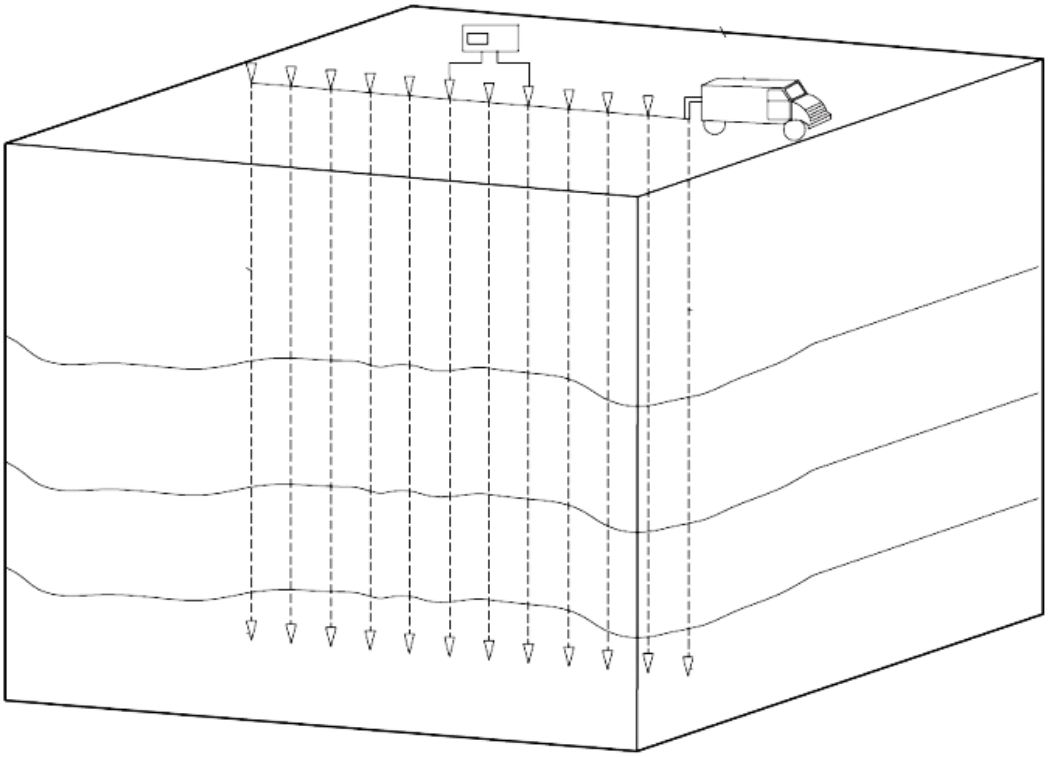

Figure 1

Schematic diagram of the MERIT method. The electrodes are planted on the surface and at depth using the direct push technology (after Harro and Kruse 2013).

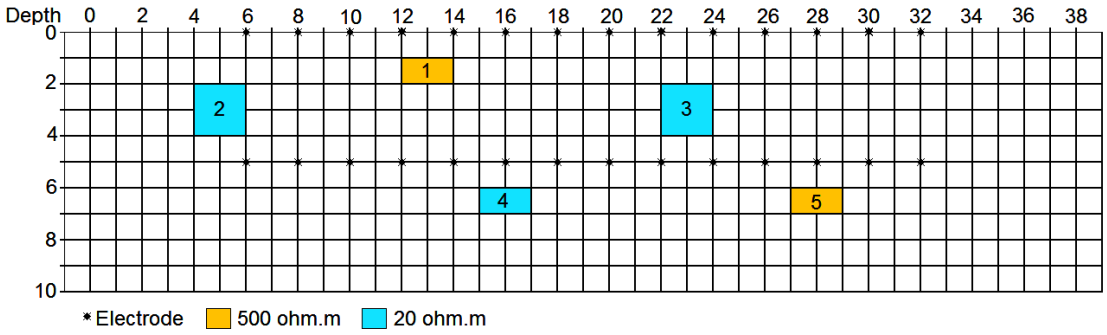

Figure 2

Layout of electrodes and arrangement of model cells used to generate the test configurations. The model used for the synthetic test data set with rectangular blocks of 20 and 500 ohm.m embedded in a background medium with a resistivity of 100 ohm.m is also shown.

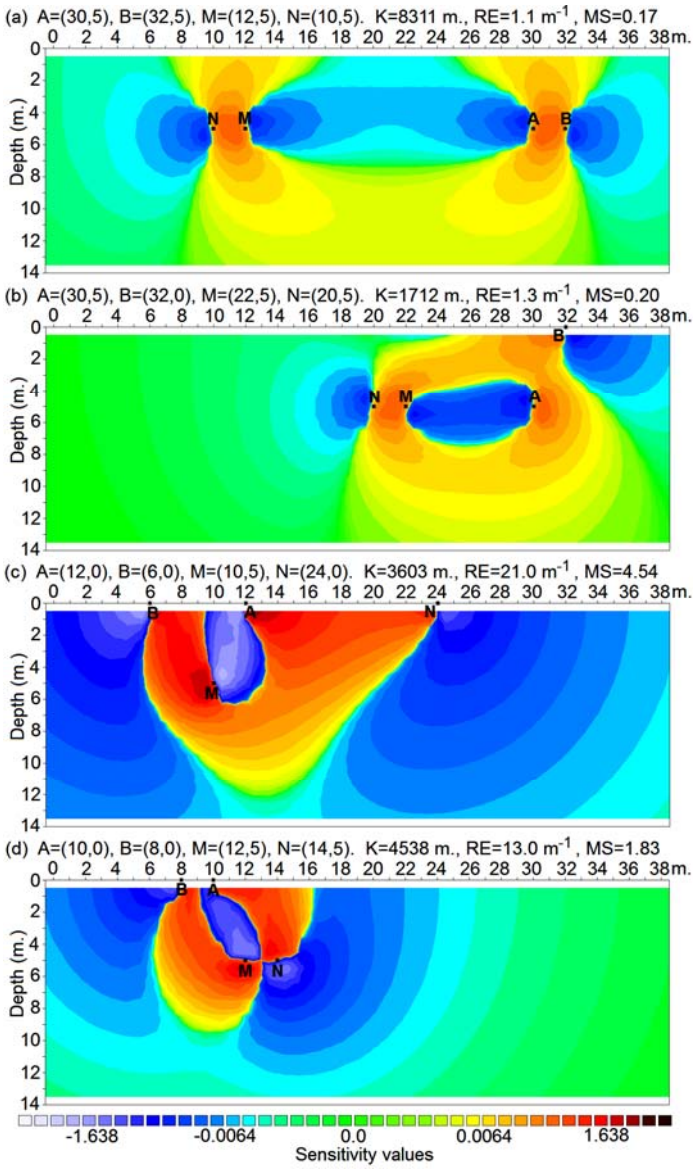

Figure 3

Sensitivity plots for stable configurations with (a) all four electrodes along the same line at 5 m depth, and (b) one current electrode on the surface and three other electrodes at 5 m depth. Sensitivity plots for unstable configurations with (c) three electrodes on the surface and one potential electrode at 5 m depth, and (d) current electrodes on the surface and potential electrodes at 5 m depth. K=geometric factor (m), R_E=geometric factor relative error (m^{-1}), MS = maximum cell sensitivity value.

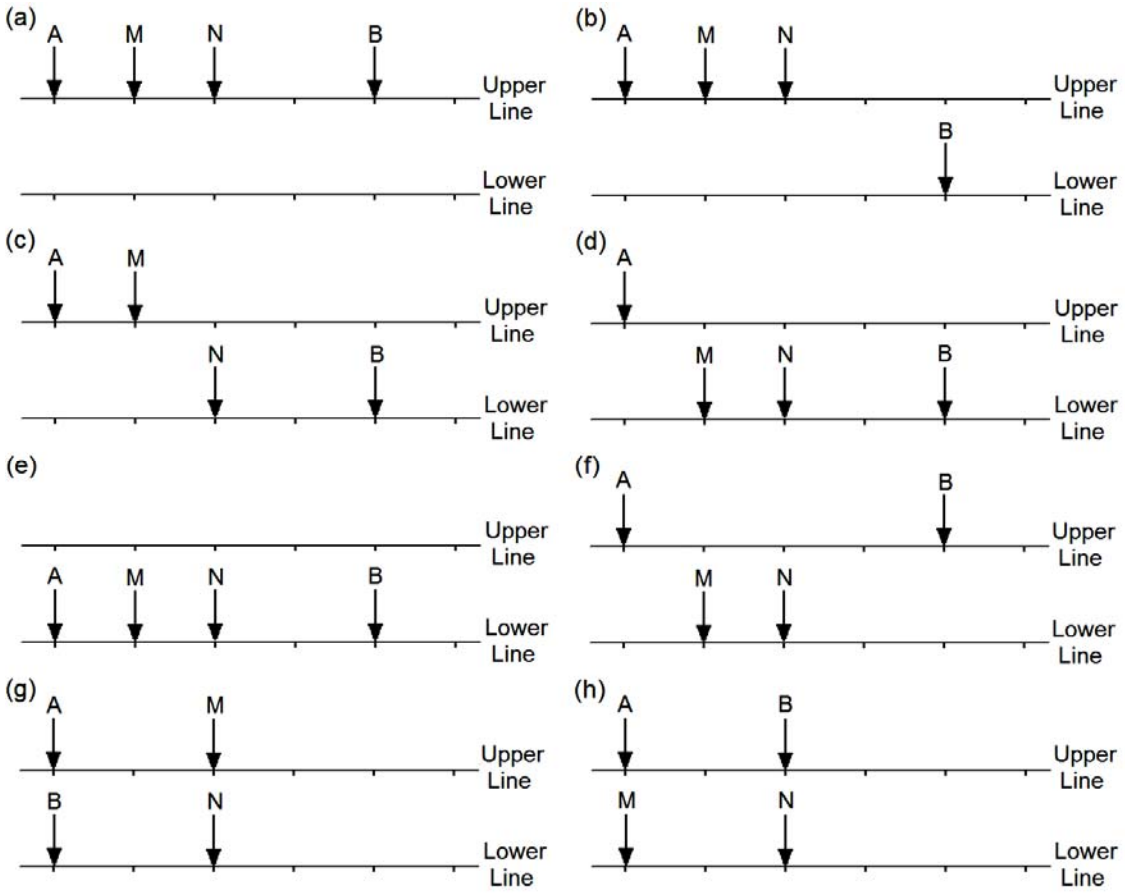

Figure 4

Examples of arrays configurations used. (a) to (e) show the different configurations of the 'alpha' type that are generated by gradually shifting the electrodes from the upper to the lower line. (f) shows an alternative alpha configuration with only the M and N electrodes in the lower line. (g) and (h) shows configurations of the 'equatorial dipole-dipole' type.

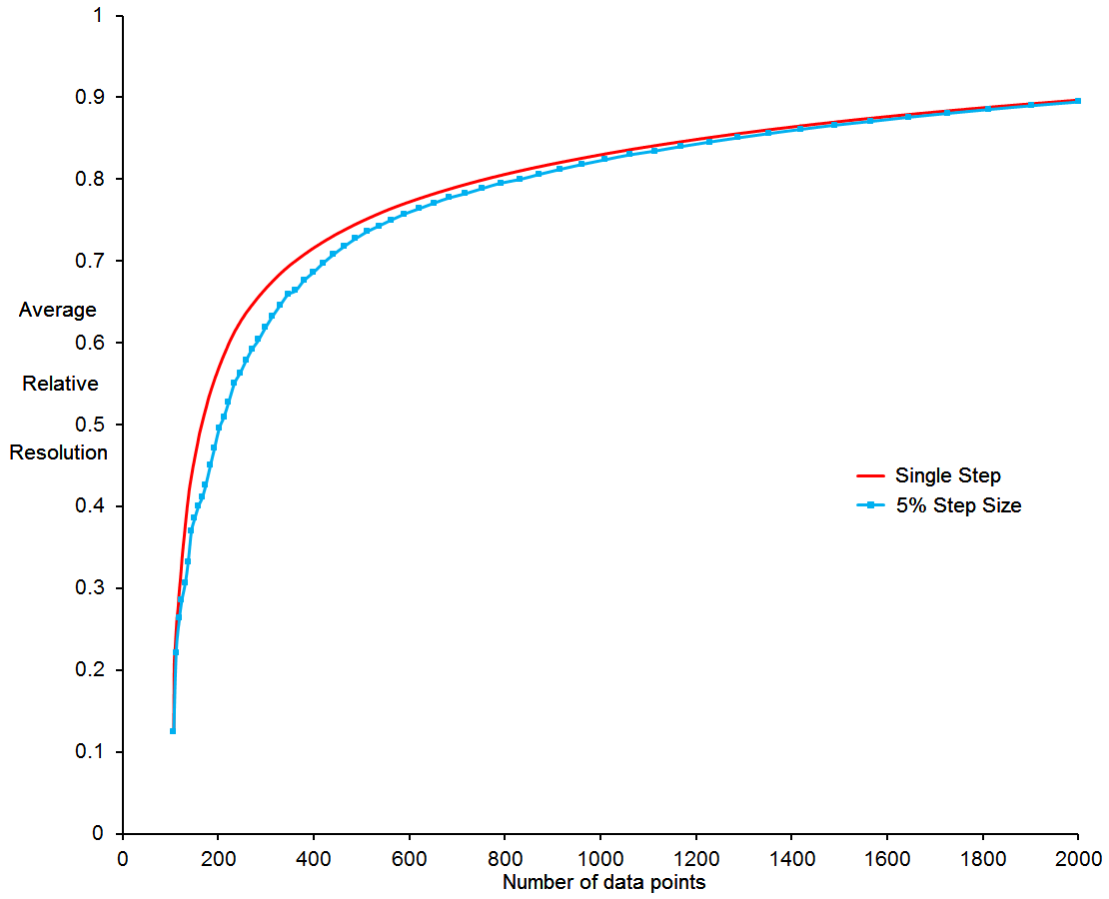

Figure 5

Change of the average relative model resolution with number of data points in the optimized data sets generated with using the single-step and block (with 5% step size) algorithms.

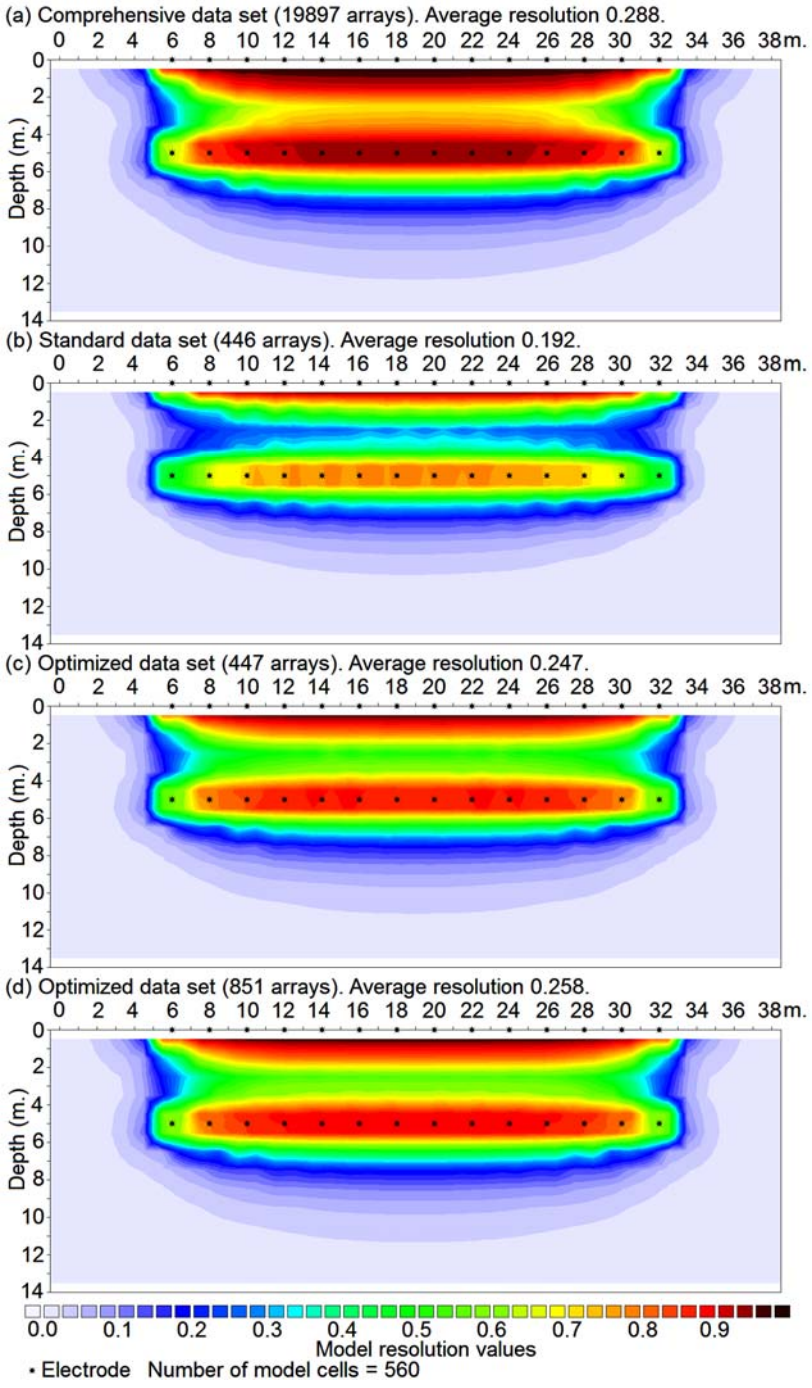

Figure 6

Model resolution sections for (a) the comprehensive data set with 19897 arrays, (b) a 'standard' measurement sequence' with 446 arrays, optimized data sets with (c) 447 and (d) 851 arrays.

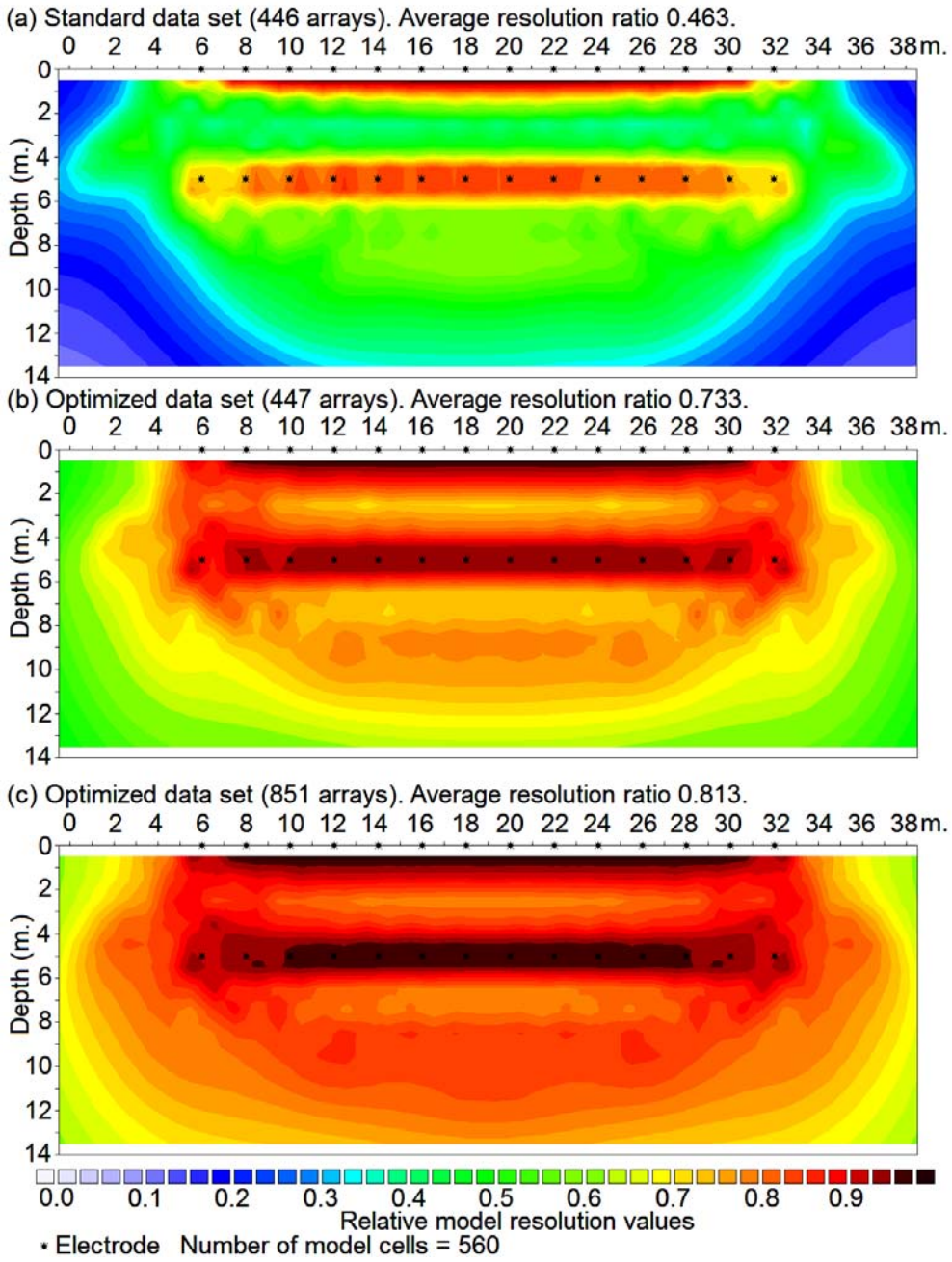

Figure 7

Relative model resolution sections for (a) a 'standard' measurement sequence with 446 data points, and optimized data sets with (b) 447 and (c) 851 data points. The sections show the ratio of the model resolution of the data set with the resolution of the comprehensive data set with 19897 arrays.

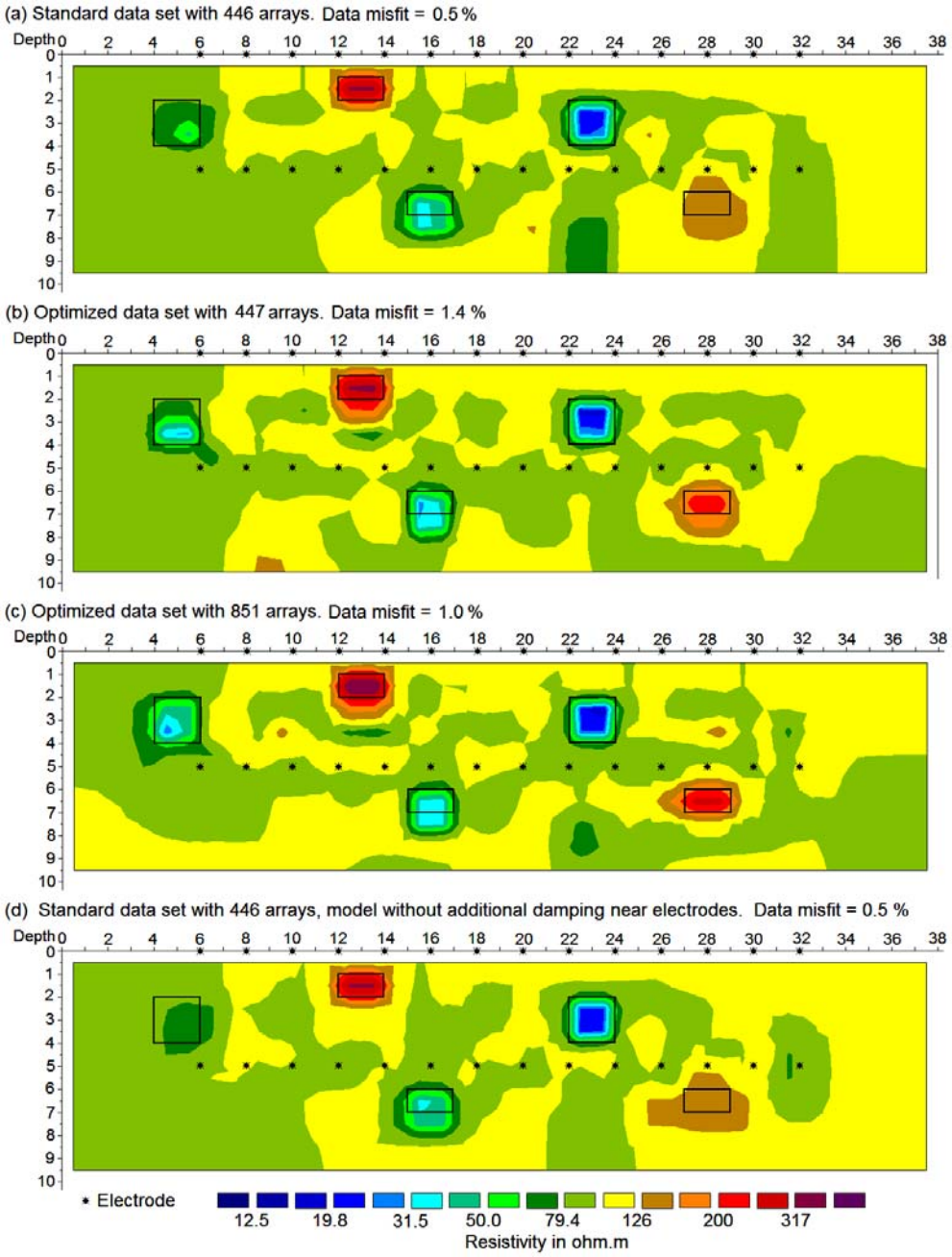

Figure 8

Inversion models for (a) standard arrays data set, optimized data sets with (b) 447 and (c) 851 data points. (d) Inversion model for standard data set without additional damping near the electrodes. The outlines of the rectangular blocks are also shown for comparison.

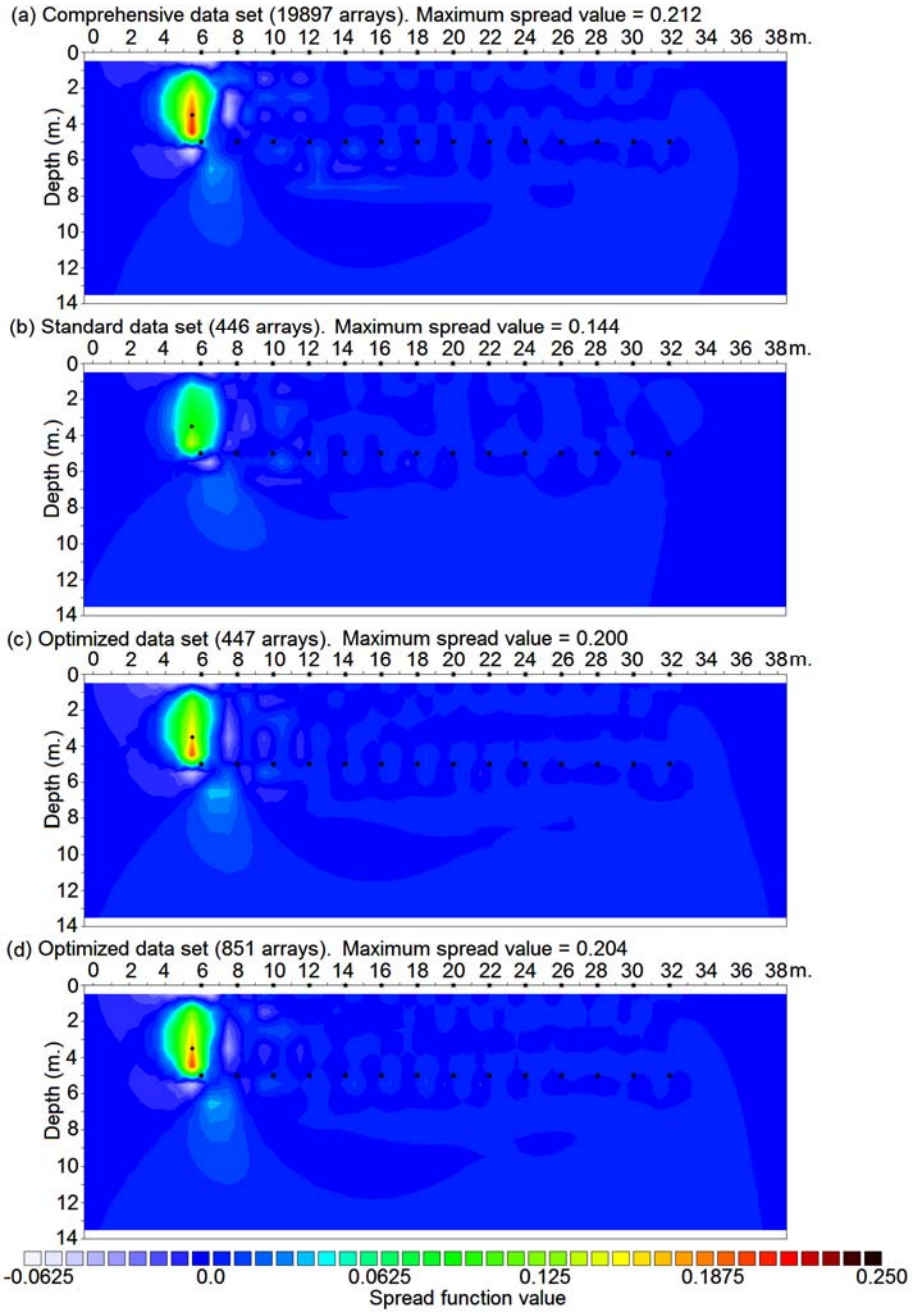

Figure 9.

Spread function plots for a model cell with center at (5.5,3.5) for (a) comprehensive data set with 19897 arrays, (b) standard data set with 446 arrays, optimized data sets with (c) 447 arrays and (d) 851 arrays.

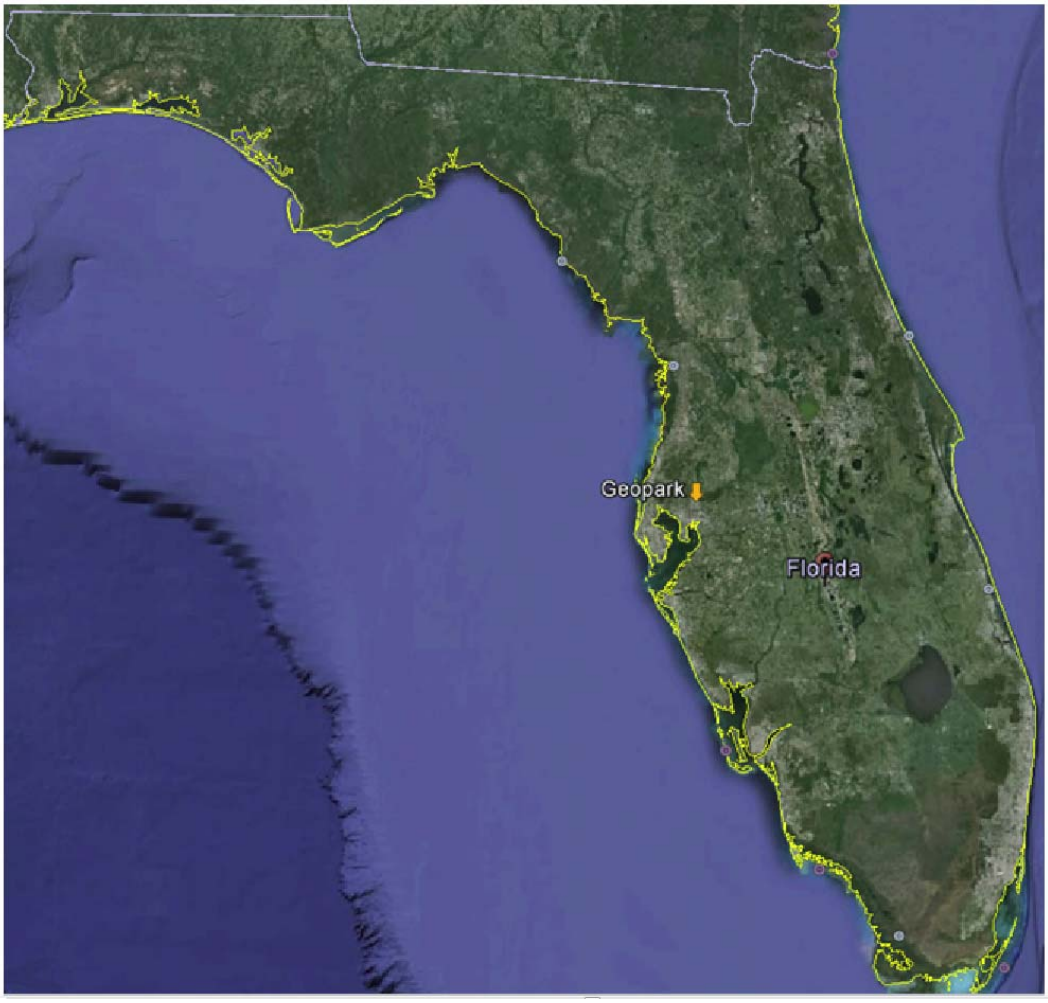

Figure 10.

Location of study site at the University of South Florida (USF).

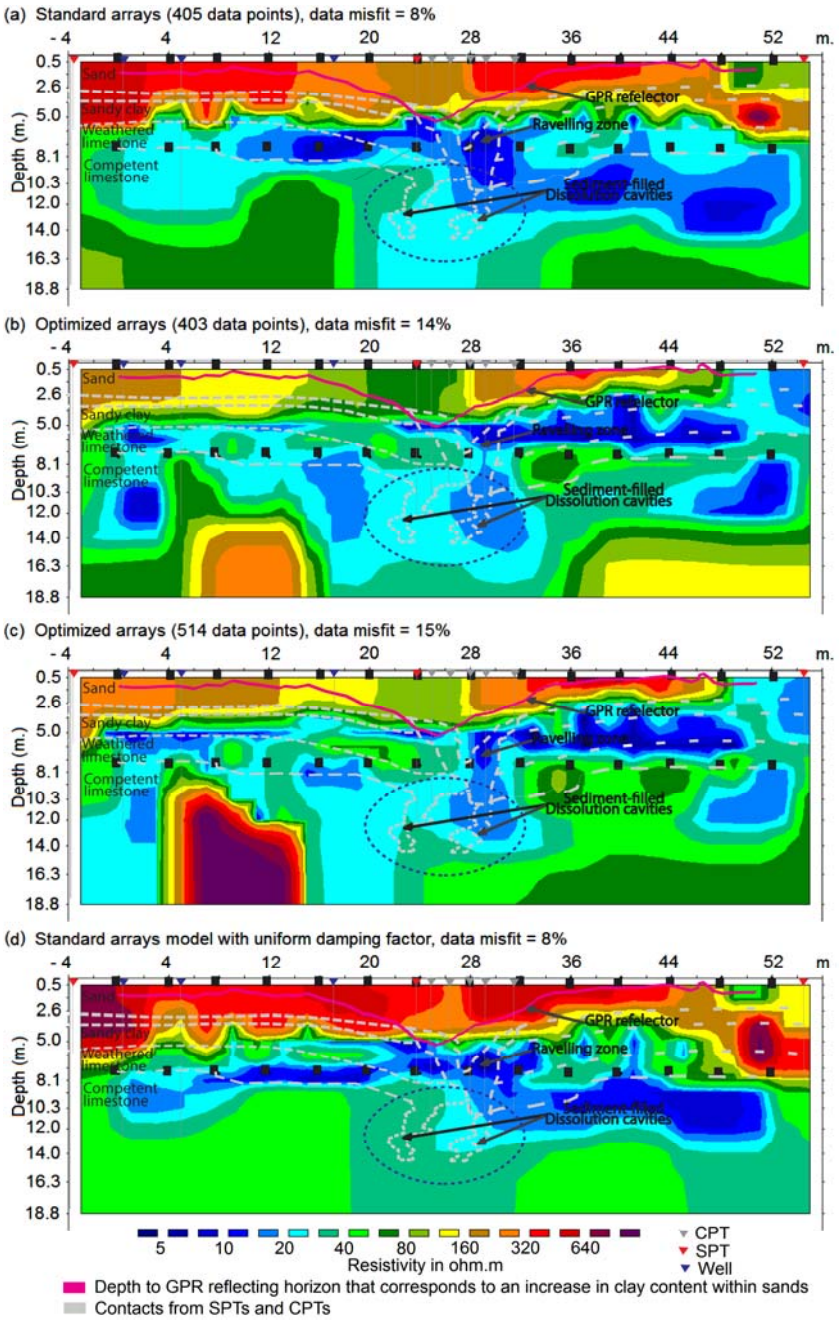

Figure 11.

Inversion models for the different data sets for the data collected with electrodes at surface and 7.62 m depth with 4 m horizontal spacing. Models for the (a) standard arrays (405 data points), optimized arrays with (b) 403 and (c) 514 data points. (d) Standard arrays model with uniform damping factor.